Proceedings of the ASME 2018
Dynamic Systems and Control Conference
DSCC2018
September 30-October 3, 2018, Atlanta, Georgia, USA

DSCC2018-9131

MODELING AND OPTIMAL CONTROL OF MICRO-CSP AND A BUILDING HVAC SYSTEM TO MINIMIZE ELECTRICITY COST

Chethan R. Reddy*
Michigan Technological University
Houghton, Michigan 49931
Email: creddy@mtu.edu

Mohamed Toub
Mohammadia School of Engineering
Mohammed V University of Rabat, Morocco
Email: mohamedtoub@research.emi.ac.ma

Meysam Razmara
Michigan Technological University
Houghton, Michigan 49931
Email: mrazmara@mtu.edu

Mahdi Shahbakhti
Michigan Technological University
Houghton, Michigan 49931
Email: mahdish@mtu.edu

Rush D. Robinett III
Michigan Technological University
Houghton, Michigan 49931
Email: rdrobine@mtu.edu

Ghassane Aniba
Mohammadia School of Engineering
Mohammed V University of Rabat, Morocco
Email: ghassane@emi.ac.ma

ABSTRACT

This paper presents a model predictive control (MPC) framework to minimize the energy cost associated with the building heating, ventilation, and air-conditioning (HVAC) system integrated with a micro-scale concentrated solar power (MicroCSP) system. To this end, a MicroCSP model is developed and then integrated to the building model of an office building in Michigan Technological University. Then, an MPC framework is designed to optimize MicroCSP electrical and thermal energy flows for HVAC use in the building. The optimal control results show that the designed MPC framework reduces the HVAC energy cost by 37-42% for a sample sunny day by optimally utilizing the solar energy, compared to the HVAC system without MicroCSP with an MPC controller. The cost saving varies from 12% to 47% depending on seasonal weather variations.

NOMENCLATURE

Symbols

θ	Incidence angle (rad)
δ	Declination angle (rad)
ω	Hour angle (rad)
$\dot{Q}$	Rate of heat flow (W)
η	Efficiency (-)
IAM	Incidence angle modifier (-)
A_p	Aperture area (m^2)
a	Heat loss coefficient (-)
T	Temperature (K)
P	Power (W)
ρ	Density (kg/m^3)
SOC	State of charge for TES (%)
C	Capacity of TES (J)
$\dot{m}$	Rate of mass flow (kg/s)
h	Enthalpy (J/kg.K)
c_p	Specific heat at constant pressure (J/kg.K)
λ_F	Power coefficient of the HVAC fan ($W.s^3/kg^3$)
COP	Coefficient of performance (-)
N_{zones}	Number of zones (-)
ERE	Energy recovery effectiveness (-)
r_p	Pressure ratio (-)
Ω	Locational marginal price ($/J)
α	Weight factor of the optimization soft constraints (-)

I. INTRODUCTION

The fossil fuels scarcity and the impact of greenhouse gas (GHG) emissions on the environment are two major challenges that the 21st-century world is confronted with. According to the

*Address all correspondence to this author.

United States Environmental Protection Agency (EPA) [1], 34% of the total CO2 emissions in the US in 2015 was caused by electricity generation. Commercial buildings accounted for 37% of total electricity consumption in the US in 2017 [2]. Half of the energy consumption in commercial buildings in the US in 2017 was caused by the heating, ventilation, and air-conditioning (HVAC) systems [3]. Hence, the considerable amount of energy consumption and associated CO2 emissions from HVAC systems in commercial buildings makes them a good candidate for energy efficiency programs.

Solar energy, as a renewable source, has a great potential in reducing the energy consumption from non-renewable sources like fossil fuels and reducing CO2 emissions. Solar energy can be converted directly to electricity using photovoltaic (PV) panels, or converted to thermal energy by using parabolic trough collectors (PTC). The thermal energy from PTC can be used for heating or used in power generators to produce electricity in a concentrated solar power (CSP) plant. Results from a study in reference [4] suggest that the entire yearly energy needed by all the world's citizens can be met by using only 0.1% of the earth's land space covered by solar collectors with merely 20% efficiency. CSP plants have been utilized over the past four decades; however, micro-scale concentrated solar power (MicroCSP) systems with power less than 1 MW have become more popular in recent years [5]. One of the well-known technologies in MicroCSP is the use of Organic Rankine Cycle (ORC) to convert low-grade thermal energy into electrical energy [6]. MicroCSP is a promising technology for use in buildings and HVAC systems, particularly for heating purposes.

The growth in electrical energy consumption and time-varying power demand by consumers have motivated energy utility companies to set variable energy cost, called the locational marginal price (LMP), according to the daily temporal energy demand and supply [7]. Therefore, an optimal reduction in energy consumption might not translate to optimal reduction in energy cost due to varying LMP. Hence it becomes necessary to control the dispatch of the renewable energy in accordance with the LMP to optimally reduce energy cost.

Solar energy, being limited to daylight hours needs to be stored in order to be dispatched according to the building HVAC demand and LMP. Therefore, in the MicroCSP plant in this study, solar energy absorbed by the PTC is converted to thermal energy. This thermal energy is stored in a thermal energy storage (TES) so that it can be dispatched to the ORC when needed. The ORC produces electricity and cogenerated low-grade heat. This low-grade heat is used to preheat the fresh air coming from the Energy Recovery Ventilator (ERV) and/or the recycled air from the rooms in the building. In addition, electrical energy contribution of the ORC reduces the electrical energy consumption from the grid. Hence, a controller of the MicroCSP system when integrated with the building HVAC system has to optimally decide when to dispatch thermal energy from TES to ORC, using solar

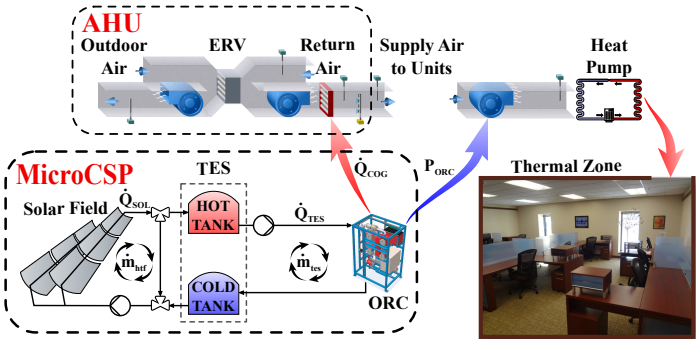

FIGURE 1. Building HVAC and MicroCSP setup in this study.

energy, and when to operate the room heat pump, using electrical energy from the grid.

Model predictive controllers (MPC) have been successfully used for control of building HVAC systems [8] with heat pumps [9], vapor compression systems [10], chillers [11], and PV panels and batteries [12, 13]. MPC can provide real-time optimal solution based on the current value and future predictions of solar irradiation, LMP, and ambient conditions while handling constraints on TES state of charge, heat pump operating limits, and meet comfort bounds in the building thermal zones. Hence in this study, we develop models of the building and MicroCSP, and design MPC to optimally control TES usage, according to the LMP, along with the thermal energy flows from the heat pumps to the building. MPC controls the room temperature based on the current and future room temperature set points and solar irradiation forecast.

To the best of authors' knowledge, this paper presents the first study undertaken for real-time MPC design to optimally reduce the energy cost by integration of MicroCSP into a building HVAC system. This paper presents optimization results for showing energy cost saving potential by optimal use of a MicroCSP system for building HVAC systems. The building model and HVAC model are based on a real test setup at Michigan Technological University and the MicroCSP model is based on our recently purchased system [14].

The building and the MicroCSP testbed is detailed in Section II. Then, the mathematical models of the PTC, TES, ORC, building thermal network, and the Air Handling Unit (AHU) are explained in Section III. The optimization problem formulation and the MPC design are described in Section IV. In Section V, the results of the building predictive control with MPC are presented and compared to the building HVAC control. In addition, a probabilistic analysis is performed to assess the effect of prediction uncertainties and seasonal variation in building energy cost saving using a MicroCSP system. Section VI summarizes the findings from this paper and Section VII discusses the planned future work.

II. TEST BED

The building considered in this work is the Lakeshore Center building at Michigan Technological University. This three-story

TABLE 1. Specifications of the MicroCSP sub-systems in this study.

System	Manufacturer/ Model number	Property	Value
PTC	Soltigua PTMx24	Area	54 m^2
		Number	2
TES	Azolis* Two-tank	HTF	Therminol VP-1
		Temperature	140-180 ^oC
ORC	ENOGIA ENO-10LT	Volume	5170 Liter
		WF	R245fa

* Contractor for installing the 2 tank TES system.

office building has an area of 61,500 ft^2 where each room or office has its individual heat pump for heating purposes. Each room is considered as an individual thermal zone in the testbed and is equipped with a thermocouple with $\pm 0.2^{\circ}C$ accuracy. The temperature data is recorded with 1-minute sampling time. The heat pumps (HPs) in this study have a nominal Coefficient of Performance (COP) of 3.2.

The details of the MicroCSP sub-systems in this study are detailed in Table 1. In the MicroCSP, solar energy is converted to thermal energy by the PTC ($\dot{Q}_{SOL}$) and is then stored in the TES. This stored thermal energy ($\dot{Q}_{TES}$) is delivered to the ORC, which cogenerates electrical power (P_{ORC}) and thermal power ($\dot{Q}_{COG}$), as shown in Fig. 1.

The HP is supplied with air from the AHU, as shown in Fig. 1. When the room is unoccupied, the air from the room is recirculated to AHU. In the AHU, air is heated by the cogenerated thermal power ($\dot{Q}_{COG}$) of the ORC when the ERV is off. When the room is occupied, the ERV is switched on and fresh air from outside is mixed with air from the room and this total air is heated by the cogenerated thermal power ($\dot{Q}_{COG}$) of the ORC.

III. MODELING

A. Parabolic Trough Collectors (PTC) Model

The solar field considered in this paper is composed of two rows of PTC PTMx-24 from Soltigua [15]. A tracking system allows the collectors to track the sun from east to west around a horizontal north-south axis. Equation (1) shows the relationship between the declination angle (δ), the zenith angle (θ_z), the hour angle (ω), and the incidence angle (θ) which is the angle between the solar beam and the line normal to the tracking plane [16] (See Fig. 2).

$$\cos(\theta) = \sqrt{\cos^2(\delta)\cos^2(\omega) + \cos^2(\theta_z)} \tag{1}$$

The declination, zenith and the hour angles are calculated according to the references [17, 18].

After finding the incidence angle, the solar power absorbed ($\dot{Q}_{gain}$) by the collectors is calculated by:

$$\dot{Q}_{gain} = \eta_o \times IAM \times \cos(\theta) \times A_p \times DNI \tag{2}$$

where, DNI is the direct normal irradiation, A_p is the aperture area, $\eta_o = 0.748$ is the collectors' optical efficiency specified by the manufacturer [15], and IAM is the incident angle modifier that correlates the losses related to the imperfection of the reflectors.

Equation (3) is a correlation used to predict the heat loss in the collectors [19]:

$$\dot{Q}_{loss} = a \times \frac{(T_{htf} - T_{amb})}{DNI} \tag{3}$$

where, $a = 0.64$ is the heat loss coefficient given by the collectors manufacturer [15], and T_{amb} is the ambient temperature. Assuming that the heat transfer fluid (HTF) temperature is linear along the collectors, we consider T_{htf} as the average temperature of the HTF in the collectors.

$$T_{htf} = \frac{T_{htf,in} + T_{htf,out}}{2} \tag{4}$$

Where, $T_{htf,in}$ and $T_{htf,out}$ are the HTF inlet and outlet temperatures of the solar field, respectively.

Finally, the heat power produced by the solar field is

$$\dot{Q}_{SOL} = \dot{Q}_{gain} - \dot{Q}_{loss} \tag{5}$$

It should be noted that the mass flow rate of the HTF ($\dot{m}_{htf}$) is controlled to increase the HTF temperature in the solar field by $\Delta T = 40^{\circ}C$ (i.e., $T_{htf,in} = 140^{\circ}C$, $T_{htf,out} = 180^{\circ}C$).

The power consumption of the solar field recirculator is given by

$$P_{recir} = \frac{P_{htf}}{\eta_{recir}} \tag{6}$$

where, η_{recir} is the recirculator efficiency, P_{htf} is the power required for recirculating the HTF and is calculated by:

$$P_{htf} = \dot{m}_{htf} . \frac{\Delta P}{\rho_{htf}} \tag{7}$$

where ρ_{htf} is the density of the HTF.

The correlation that estimates the pressure drop in the solar field (ΔP) is given in the collectors' data sheet [15]. The collector model was validated using the experimental data provided by the manufacturer Soltigua for the PTMx-24 [20].

B. Thermal Energy Storage (TES) Model

In this paper, the TES system stores the energy from the solar field so that it can be used when there is a demand for thermal and electrical energy by the building. In general, TES is used to mitigate intermittent power generation and ensure reliable and uninterrupted power supply through ORC in the event of temporary weather changes. For our study, a two-tank direct system is considered as the TES (Fig. 1). Both tanks are modeled as a fully-mixed cylindrical tank with a constant cross-sectional area. The TES contains a variable quantity of the HTF and have the capacity to store the whole volume of HTF. During charging, the hot tank accumulates the high-temperature HTF produced by the

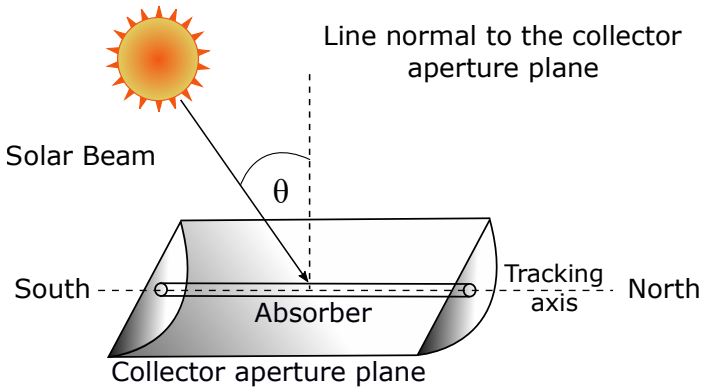

FIGURE 2. Schematic of Parabolic Trough Collectors (PTC), showing the incidence angle (θ).

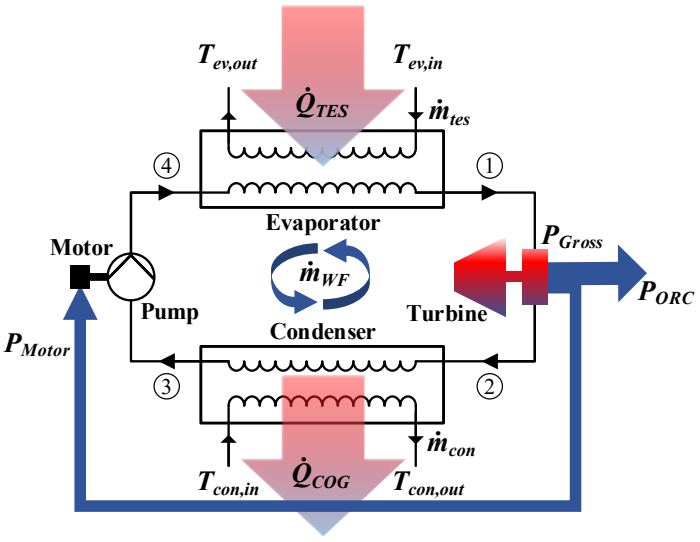

FIGURE 3. Schematic of the Organic Rankine Cycle (ORC) in this study.

solar field, while the cold tank sends back the low-temperature HTF to the solar field. During discharging, the hot tank supplies the high-temperature HTF to the power cycle which uses the HTF thermal energy to produce electricity and low-grade heat and directs the low-temperature HTF to the cold tank.

The state of charge (SOC) of the TES is calculated using the following equation:

$$S\dot{O}C = \frac{\dot{Q}_{SOL} - \dot{Q}_{TES}}{C_{TES}} \tag{8}$$

where, $\dot{Q}_{SOL}$ is the thermal power produced by the solar field, $\dot{Q}_{TES}$ is the power from the TES to the ORC, and C_{TES} is the capacity of the TES.

C. Organic Rankine Cycle (ORC) Model

This work uses the ORC system ENO-10LT manufactured by ENOGIA [14]. This system is a low-temperature 10 kW ORC module, which uses R245fa as the working fluid (WF).

The schematic of the ORC system in this study is shown in Fig. 3. The WF enters the turbine in a vapor state at high pressure and high temperature (State 1 in Fig. 3). The high pressure fluid energy is converted to mechanical energy in turbine and then converted to electrical energy in the power generator. After passing the turbine blades, the WF remains at its vapor state at a lower temperature and pressure (State 2 in Fig. 3). Then, the WF enters the condenser where its state changes to liquid and thereby rejecting heat through the heat exchanger (State 3 in Fig. 3). This heat will be used to heat the fresh air coming from the ERV and/or the recycled air from the rooms. The low temperature and low pressure liquid is then compressed by a pump (driven by a motor) to increase its pressure (State 4 in Fig. 3). The cycle is repeated when the WF passes through the evaporator and acquires heat extracted from the HTF coming from the TES, which changes the state to vapor and increases its temperature.

Applying the First Law of Thermodynamics for the ORC as a closed system yields:

$$P_{gross} = \eta_{gen} \times \dot{m}_{WF} \times (h_1 - h_2) \tag{9a}$$

$$P_{motor} = \frac{\dot{m}_{WF} \times (h_4 - h_3)}{\eta_{motor}} \tag{9b}$$

$$P_{ORC} = P_{gross} - P_{motor} \tag{9c}$$

$$\dot{Q}_{COG} = \dot{m}_{WF} \times (h_2 - h_3) \tag{9d}$$

$$\dot{Q}_{TES} = \dot{m}_{tes} \times c_{p,htf} \times (T_{ev,in} - T_{ev,out}) \tag{9e}$$

where, P_{gross} is the gross electrical power generated by the turbine, P_{motor} is the electrical power consumed by the motor, P_{ORC} is the net electrical power generated by the ORC, $\dot{Q}_{COG}$ is the cogeneration heat rate delivered by the ORC, $\dot{Q}_{TES}$ is the heat rate from the HTF to the ORC evaporator, h_x is the enthalpy at state x, η_{gen} and η_{motor} are the efficiencies of the ORC turbine generator and motor, respectively, $\dot{m}_{tes}$ is the HTF mass flow rate from the TES, $T_{ev,in}$ and $T_{ev,out}$ are the HTF inlet and outlet temperatures to the ORC evaporator, respectively.

It can be shown that

$$P_{ORC} = f(\dot{m}_{WF}, \dot{m}_{tes}, c_{p,htf}, T_{ev,in}, T_{ev,out}, h_3, r_p, \eta_{gen}, \eta_{motor}) \tag{10a}$$

$$\dot{Q}_{COG} = g(\dot{m}_{WF}, \dot{m}_{tes}, c_{p,htf}, T_{ev,in}, T_{ev,out}, h_3, r_p, \eta_{gen}, \eta_{motor}) \tag{10b}$$

where, r_p is the pressure ratio of the ORC turbine.

The mass flow rate, $\dot{m}_{WF}$ is kept constant in the ORC module in this study; $T_{ev,in}$ and $T_{ev,out}$ are constant design temperatures, $c_{p,htf}$ is considered constant. In addition, h_3 is a function of T_3 and P_3 which are the condensation temperature and pressure, that are kept constant by controlling the coolant mass flow rate. η_{gen},

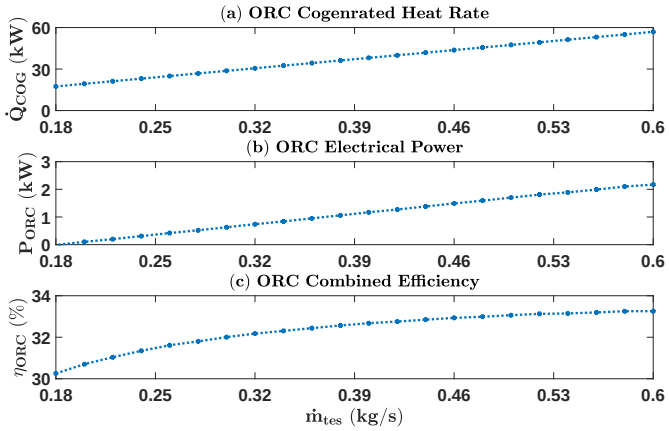

FIGURE 4. ORC cogeneration heat production rate ($\dot{Q}_{COG}$), electric power (P_{ORC}), and combined efficiency (η_{ORC}) as a function of HTF mass flow rate from TES ($\dot{m}_{tes}$).

and η_{motor} are constant for the given system. The r_p is variable according to the power needed and is fixed to a nominal value of 3 to increase combined efficiency (η_{ORC}) in the ORC working range. By considering all the assumption above, the combined efficiency (η_{ORC}) of the ORC in this study is calculated by:

$$\eta_{ORC} = \frac{(P_{ORC} + \frac{\dot{Q}_{ORC}}{COP})}{\dot{Q}_{TES}} \times 100 \tag{11}$$

where, COP is the coefficient of performance (COP) of HPs. Thus, P_{ORC} and $\dot{Q}_{COG}$ are functions of $\dot{m}_{tes}$ for the ORC system in this study. The variation of P_{ORC}, $\dot{Q}_{COG}$, and η_{ORC} as a function of $\dot{m}_{tes}$ is shown in Fig. 4. The mathematical model in this work was validated against experimental data [21] from the manufacturer and the errors for estimating P_{ORC} and $\dot{Q}_{COG}$ were found to be less than 10%.

D. Building Thermal Model

The building testbed presented in section II (i.e., Lakeshore Center at Michigan Technological University) is modeled by using the well-known RC modeling approach where heat storage and heat transfer between adjacent zones and outdoor are modeled with capacitive, resistive, and current elements. The details of the building testbed modeling and experimental validation are found in our previous works in [22–24].

The building HVAC energy consumption is represented by the energy index ($I_{e,t}$) which is calculated as follows

$$I_{e,t} = \sum_{t=0}^{t} \sum_{i=1}^{N_{zones}} \left(P^F_{i,t} + P^H_{i,t}\right) \times \Delta t \tag{12}$$

where, t is time, i is the zone number, N_{zones} is the total number of building thermal zones. Since this work concentrates on the heating mode, the power consumed by the building HVAC

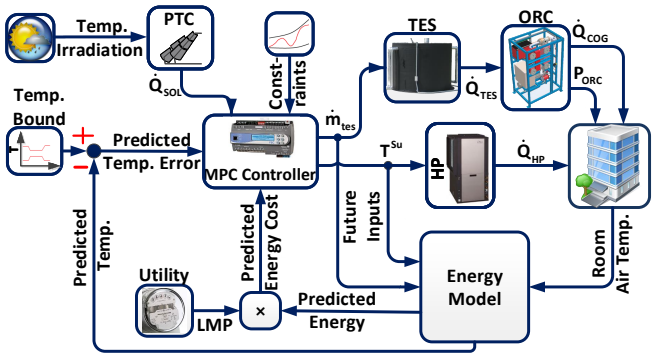

FIGURE 5. Schematic of the designed MPC to minimize the operational cost of the combined MicroCSP and building HVAC system.

system is the sum of the ventilation fan power ($P^F_{i,t}$) and the HPs electrical power consumption ($P^H_{i,t}$). The HVAC electrical power consumption is calculated by:

$$P^F_{i,t} = \gamma_F . (\dot{m}^r_{i,t})^3 \tag{13a}$$

$$P^H_{i,t} = \frac{\dot{m}^r_{i,t} . c_{p,air} . (T^{Su}_{i,t} - T^{AHU}_{i,t})}{COP} \tag{13b}$$

where, γ_F is power coefficient of the fan and $\dot{m}^r_i$ is the mass flow rate of the supply air to each room. Equation (13b) calculates the power consumption of the HPs as a function of the supply air temperature (T^{Su}), the HPs inlet temperatures ($T^{AHU}_{i,t}$), and the COP of the HPs.

E. Air Handling Unit (AHU) Model

The AHU (Fig. 1) feeds preheated air to the HPs. The outlet air from the AHU is distributed equally to all the zones and this distributed air is inlet to the HP at each zone. The inlet air temperature to the HP is calculated by Equation (14) for both occupancy and non-occupancy modes.

$$T^{AHU}_{i,t} = \begin{cases} \text{occupancy mode,} \\ \dfrac{\dot{m}^r_{i,t} - \dot{m}^v_{i,t}}{\dot{m}^r_{i,t}} T^r_{i,t} + \dfrac{\dot{m}^v_{i,t}}{\dot{m}^r_{i,t}} T^{ERV}_t + \dfrac{\dot{Q}_{COG,t}}{N_{zones} \dot{m}^r_{i,t} c_{p,air}} \\ \text{non-occupancy mode,} \\ T^r_{i,t} + \dfrac{\dot{Q}_{COG,t}}{N_{zones} \dot{m}^r_{i,t} c_{p,air}} \end{cases} \tag{14}$$

In the non-occupancy mode, the returning air from the zones is recirculated through the ORC condenser then goes to the HPs. In the occupancy mode, the ventilation requirement is considered according to the ANSI/ASHRAE Standard 62.1-2007 for required indoor air quality. In this work, the default occupant den-

sity of an office space is 5 persons/100 m^2 and the default combined outdoor air rate (i.e., required fresh air) is 8.5 L/(s.person), using the ASHRAE standard. Hence, the returning air from the zones is recirculated and mixed with the minimum required mass flow rate ($\dot{m}_i^v$) of fresh air from the ERV. Then, the resulting air goes through the ORC condenser and is heated to supply the HPs or the zones directly. The temperature of the ERV outlet in Equation (15) is calculated using the Energy Recovery Effectiveness (ERE) defined by ASHRAE Standard 84 and AHRI Standard 1060.

$$T_t^{ERV} = T_{amb,t} + ERE.(T_{i,t}^r - T_{amb,t}) \tag{15}$$

IV. BUILDING MODEL PREDICTIVE CONTROL

Fig. 5 depicts the structure of our designed MPC for optimal energy cost control of the building with the MicroCSP system. To minimize the HVAC energy cost of the building, the objective function is defined according to Equation (16) subject to the constraints listed in Equation (17). The optimization problem is solved at each time step t to find the N future values of the two inputs, including the supply air temperature (T^{su}) and the HTF mass flow rate from the TES ($\dot{m}_{tes}$). Here, room temperature soft constraints are used to guarantee feasibility of optimal solution at all times. The MPC optimization model inputs are weather forecast and irradiation. Room air temperature bounds and ventilation requirements are set according to ANSI/ASHRAE Standard 55-2013 and ANSI/ASHRAE Standard 62.1-2007, respectively.

$$\min_{\dot{m}_{tes},T^{su},\bar{\varepsilon},\underline{\varepsilon}} \{\overbrace{(I_{e,t} - \sum_{t=0}^{t} P_{ORC,t}.\Delta t)}^{P_{Grid,t}.\Delta t} \times \Omega_t + \alpha(|\bar{\varepsilon}|_1 + |\underline{\varepsilon}|_1)\} \tag{16}$$

Subject to the following constraints:

$$T_{t+k+1|t} = AT_{t+k|t} + BT_{t+k|t}^{Su} + Ed_{t+k|t} \tag{17a}$$

$$T_{t+k|t}^r = CT_{t+k|t} \tag{17b}$$

$$P_{ORC,t+k|t} = f(\dot{m}_{tes_{t+k|t}}) \tag{17c}$$

$$\dot{Q}_{COG,t+k|t} = g(\dot{m}_{tes_{t+k|t}}) \tag{17d}$$

$$SOC_{t+k+1|t} = SOC_{t+k|t} + \frac{(\dot{Q}_{SOL_{t+k|t}} - \dot{Q}_{TES_{t+k|t}}).\Delta t}{C_{TES}} \tag{17e}$$

$$\underline{SOC} \leq SOC_{t+k|t} \leq \overline{SOC} \tag{17f}$$

$$0 \leq \dot{m}_{tes_{t+k|t}} \leq \dot{m}_{max} \tag{17g}$$

$$T_{t+k|t}^{AHU} \leq T_{t+k|t}^{Su} \leq \bar{T}_{t+k|t} \tag{17h}$$

$$\underline{T}_{t+k|t}^r - \underline{\varepsilon}_{t+k|t} \leq T_{t+k|t}^r \leq \bar{T}_{t+k|t}^r + \bar{\varepsilon}_{t+k|t} \tag{17i}$$

$$\underline{\varepsilon}_{t+k|t}, \bar{\varepsilon}_{t+k|t} \geq 0 \tag{17j}$$

Equations (17a) and (17b) represent the buildings state-space model; (17c) and (17d) constitute the ORC model; (17e) includes the TES model for calculating SOC; (17f) shows the TES lower bound $\underline{SOC}$ and upper bound $\overline{SOC}$ set to 5% and 95%, respectively; (17g) shows the ORC evaporator mass flow limit ($\dot{m}_{max}$) set by the manufacturer [14]; (17h) is the supply air temperature constraint based on HP settings; (17i) is the constraint to include desired room air temperature bound; finally, (17j) includes the slack variables constraints.

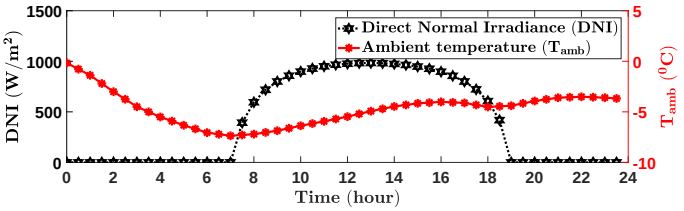

FIGURE 6. Measured Direct Normal Irradiance (*DNI*) and ambient air temperature (T_{amb}) as a function of time of the sample winter day in Houghton, MI.

V. CONTROL RESULTS

The building, solar field, and TES models are implemented in MATLAB®. LMP data from Midcontinent Independent System Operator (MISO) [25] is used. The measured solar *DNI* and the ambient temperature for a sample winter day in Houghton, MI is considered for simulations, as shown in Fig. 6. The update rate (or sample time) considered, for both Rule-Based Control (RBC) and MPC was 30 minutes.

For MPC formulation, YALMIP Toolbox [26] was used in MATLAB® which provides a symbolic syntax to interface with the solver. The prediction horizon used was 24 hours, and the default solver of YALMIP Toolbox [26], FMINCON was used. With those settings, the simulation time was 120 seconds in a laptop computer with Intel(R) Core(TM) i7-4500 CPU @ 1.80GHz and 8 GB RAM.

A. Rule-Based Control (RBC) of the building HVAC system integrated with the MicroCSP system

This section presents the results of RBC of the building HVAC system with the MicroCSP system. The RBC provides a baseline for comparison and its rules are defined as follows:

$$T_{i,t}^{Su} = \begin{cases} T_{i,t}^{AHU} \text{ if } T_{i,t}^r > \bar{T}_{i,t}^r \\ \bar{T}_{i,t} \text{ if } \underline{T}_{i,t}^r \leq T_{i,t}^r \leq \bar{T}_{i,t}^r \text{ AND } T_{i,t-1}^{Su} = \bar{T}_{i,t-1} \\ T_{i,t}^{AHU} \text{ if } \underline{T}_{i,t}^r \leq T_{i,t}^r \leq \bar{T}_{i,t}^r \text{ AND } T_{i,t-1}^{Su} < \bar{T}_{i,t-1} \\ \bar{T}_{i,t} \text{ if } T_{i,t}^r < \underline{T}_{i,t}^r \end{cases} \tag{18}$$

If the room air temperature is above the upper limit for desired air temperature of the room ($\bar{T}_{i,t}^r$), then the HP is switched off ($T_{i,t}^{Su} = T_{i,t}^{AHU}$). If the room air temperature is below the lower limit for desired air temperature of the room ($\underline{T}_{i,t}^r$), then the HP is switched on to its maximum capacity ($T_{i,t}^{Su} = \bar{T}_{i,t}$). If the room

air temperature is between the upper and lower limits for desired air temperature of the room, then to avoid chattering of HP, the HP is switched off or switched on depending on whether the HP was switched off or switched on at the previous time step.

Fig. 7(a) shows the air temperature of a sample room for a sample day. As seen from the figure, the room temperature starts at 19°C and ramps down till it reaches below the lower temperature bound. The room temperature then violates the comfort temperature bounds from hour 6.30 to 7.30. This is because the comfort temperature bounds narrow down and the supply air temperature ramp up by the HP is limited by the maximum value of supply air temperature. From hours 8.30 to 15.30, the thermal energy from PTC (Fig. 7(b)) maintains the room temperature within the comfort bounds and here the HP is switched off. Here, we do not have control of the TES, i.e. the power output of the PTC becomes the power input to the ORC. After hour 15.30, the room temperature ramps down till it reaches the lower temperature bound. Once the room temperature reaches the lower bound, the HP switches on again and ramps up the room temperature to near the upper bound. Then, the room temperature ramps down but is within the comfort bounds. The total energy consumed from the grid is multiplied with the LMP and the total energy cost is shown in Fig. 7 and Table 2.

B. Model Predictive Control (MPC) to minimize energy cost of the building HVAC system

This section presents the MPC results of the building HVAC control without the MicroCSP system. The MPC without MicroCSP provides a second baseline for comparison. The MPC framework formulation is similar to that in Equations (16) and (17) excluding (17c), (17d), (17e), (17f), and (17g) which are related to the ORC and TES models and constraints. Details about the optimal HVAC control and the optimization problem formulation can be found in [23].

Fig. 8(a) shows the air temperature for the same room and same day as Fig. 7. As seen from the figure, the room temperature is within the comfort temperature bounds. The only control variable is the supply air temperature (T^{Su}). The optimizer minimizes the energy cost of the building HVAC system by supplying heat to keep the room air temperature at sections where the LMP is lowest, as shown in Fig. 8(a). Heating supply air is done by the heat pumps which take power from the grid (Fig. 8(b)). The total energy cost is shown in Table 2, and shows 41.3% less cost, compared to RBC of the building HVAC system integrated with the MicroCSP system.

C. Model Predictive Control (MPC) to minimize energy cost of the building HVAC system integrated with the MicroCSP system

This section presents the MPC results of the building with MicroCSP integration for the same number of thermal zones studied in Sections V-A and V-B.

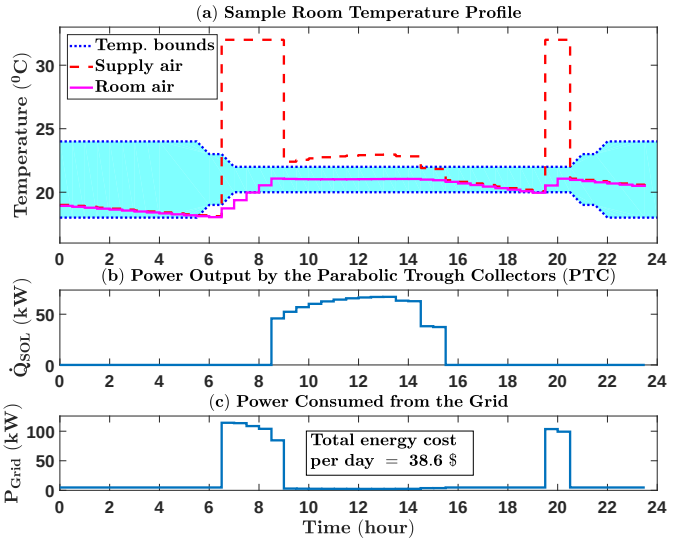

FIGURE 7. RBC results with MicroCSP integration into the building.

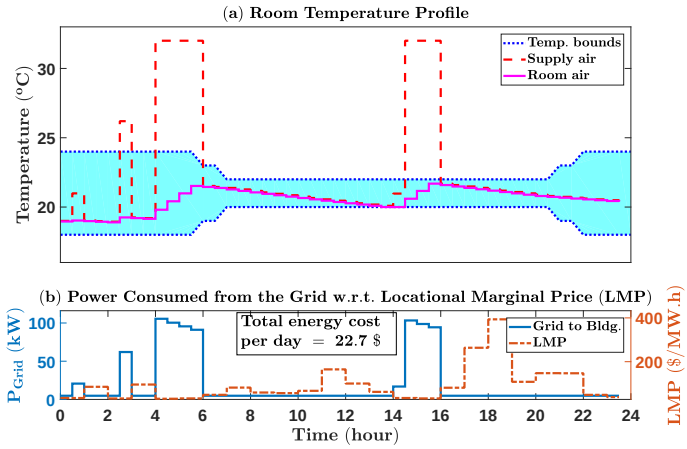

FIGURE 8. MPC results without MicroCSP integration into the building.

The supply air temperature and the room air temperature for same conditions of Fig. 7 and Fig. 8 are shown in Fig. 9(a). It can be seen that when the building is not occupied (i.e., from midnight to 4 AM), the heat pumps are shut down, while the room temperature is within the bounds. Then, during the very early morning, before the beginning of the occupancy mode and when the LMP is low, the optimizer turns on the HP for preheating to ensure that the room temperature stays within the comfort temperature bounds. To minimize HVAC energy cost of the building HVAC system, the optimizer tries to switch on the HP only when the LMP is low. Fig. 9(b) depicts the heat produced by the PTC, and the heat dispatched from the TES to the ORC. When there is no MicroCSP, all the heat required is supplied by the HP (Fig. 8). Whereas with MicroCSP, the HP supplies the required heat only during the periods when LMP is low. The TES

is charged with heat from the PTC and runs the ORC to supply cogenerated heat to the building when the LMP is high and/or when the temperature falls below the lower comfort bound. The electricity produced by the ORC is consumed by the ventilation fans (Fig. 9(c)). Fig. 9(d) shows the grid power supplied to the HP along with the LMP. The excess of heat produced by the solar field and not used by the ORC is stored in the TES, causing the SOC of the TES to increase. The stored heat is recovered later, at the end of the day when there is not enough solar irradiation at the solar field to produce heat, and the SOC diminishes until it reaches its lower bound as it can be seen in Fig. 9(e).

Table 2 provides the energy cost comparison for showing the effect of utilizing MicroCSP and design of MPC, compared to the baseline RBC for the combined HVAC and MicroCSP system. The RBC results show the maximum cost. While HVAC system without a MicroCSP leads to 41.3% energy cost saving. Furthermore, the designed MPC framework with MicroCSP leads to a 63.4% energy cost saving from the baseline and a further 37.7%, compared to MPC without MicroCSP case. The main conclusion from this comparison is that an MPC framework needs to be designed to fully take advantage of the MicroCSP thermal and electrical energies for the integration into the building HVAC system.

D. Effect of varying number of zones and TES capacity on MPC Results

The results presented so far are for a sample winter day for a building with 48 zones and for TES capacity of 96 kW.h. In this section, energy and energy cost savings from the case of without MicroCSP integration to with MicroCSP integration into the building are calculated by varying the number of zones of the building and also by varying the TES capacity.

Fig. 10(a) shows that if the number of zones of the building is increased without changing the TES capacity of the MicroCSP, then the energy cost savings have a lesser slope than energy savings. Energy saving increases with increase in the number of zones due to the combined action of MicroCSP and MPC (see difference in room temperature profiles between Fig. 8(a) and Fig. 9(a)). But the fan power of the zones (see equation (13a)), which is on throughout the day, increases with increase in number of zones and cannot be fully satisfied by the electrical output of the ORC in the periods of high LMP. This result shows the importance of proper sizing of the MicroCSP with respect to building zones.

TABLE 2. Electrical energy cost comparison.

System	Control Type	Energy Cost per day [$]	Energy Cost Saving* [%]
HVAC + MicroCSP	RBC	38.61	0
HVAC	MPC	22.67	41.3
HVAC + MicroCSP	MPC	14.12	63.4

* Energy cost saving percentage is calculated by comparison with RBC for the combined HVAC and MicroCSP system as baseline.

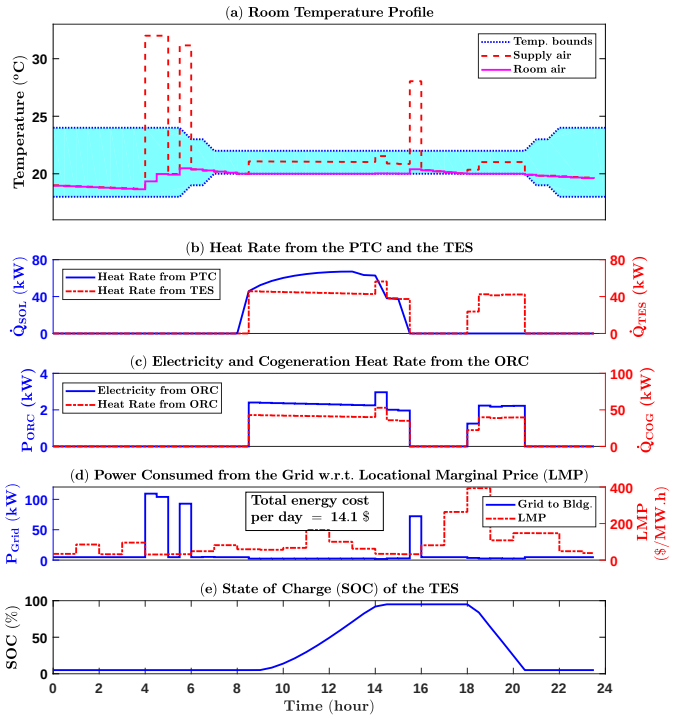

FIGURE 9. MPC results with MicroCSP integration into the building.

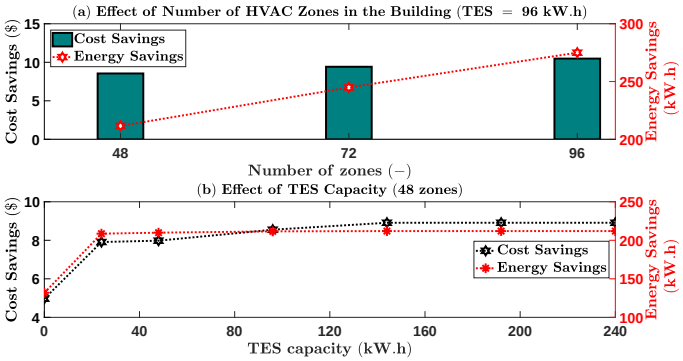

FIGURE 10. Effects of number of building HVAC zones and TES capacity for energy and energy cost savings. The savings are calculated by comparing MPC HVAC+MicroCSP and MPC HVAC operations.

Fig. 10(b) shows the importance of including a TES and the importance of TES sizing to get the maximum energy cost savings. By including TES with proper sizing both energy saving and cost saving increases by 16%, compared to not including TES. However, the energy savings remain flat above a certain TES capacity. But the energy spent is shifted with respect to LMP and will lead to higher energy cost savings until TES capacity of 144 kW.h.

E. Monte-Carlo Simulations

The results presented in Section V-C shows important savings in the HVAC energy cost of the building for the sample winter day. However, prediction uncertainty and the variation across the year in solar irradiation including the direct normal irradiance (DNI), ambient temperature (T_{amb}) and LMP were not taken into account. Hence, a probabilistic analysis using Monte-Carlo simulations is carried out to account for these uncertainties. These Monte-Carlo simulations can show possible outcomes for the energy cost savings and how likely each outcome is to happen.

Fig. 11(a) presents the probability distribution of the energy cost saving accounting for uncertainty prediction of solar irradiation, outdoor temperature, and LMP. To account for the uncertainty, an additive uncertainty with a normal distribution is considered and random numbers are generated for each factor (i.e., irradiation, outdoor temperature, and LMP) using the results from [27]. The results show that the probability of at least 38% energy cost saving is around 50%. Furthermore, Fig. 11(a) shows that in the worst case, the energy cost saving for the sample day will drop to 37%.

Fig. 11(b) presents the probability distribution of the energy cost saving accounting for seasonal variation of solar irradiation, outdoor temperature, and LMP. To account for the seasonal variation, the solar irradiation data and outdoor temperature data are taken for Houghton, MI from Sept., 2014 to Apr., 2015 from the US National Renewable Energy Lab website. [28]; for LMP the results from [27] are used. It is shown that the probability of at least 27.5% energy cost saving is around 50%. Furthermore, Fig. 11(b) shows that in the worst case, the energy cost saving for the sample day will drop to 12%.

For each Monte-Carlo Simulation, the same uncertainty value were added to the LMP and ambient temperature for both MPC simulations (i.e. with and without MicroCSP). One hundred simulations were carried out to generate the distribution in Fig. 11(a) and Fig. 11(b).

It should be noted that all the results in Section V are obtained for a sample sunny winter day in Houghton, MI in the United States. The energy cost saving percentages are anticipated to change for cloudy days and/or days with different outdoor temperatures.

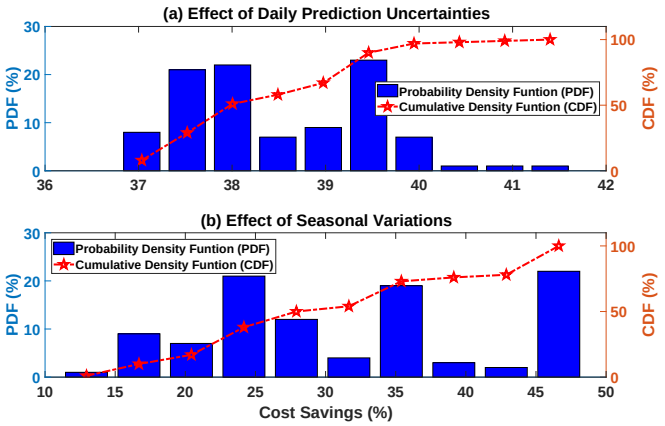

FIGURE 11. Monte-Carlo simulation results showing probability distribution of energy cost savings from the case of MPC without MicroCSP integration to the case of of MPC with MicroCSP integration into the building.

VI. SUMMARY AND CONCLUSION

This paper presented the first study undertaken to design a predictive controller to minimize energy cost for the optimal integration of a MicroCSP system into a building HVAC system. A control-oriented model was developed for a MicroCSP system integrated into a building HVAC system. The resulting model was then incorporated into an MPC framework to optimally coordinate thermal and electrical energy sources according to HVAC needs in the building. The main findings from this study, for the sample sunny winter day in Houghton, MI, include:

- The designed MPC framework can provide 63% energy cost saving, compared to a heuristically designed rule-based controller (RBC) for the combined HVAC and MicroCSP systems.
- The integration of MicroCSP to the building HVAC system with an MPC controller can reduce the HVAC energy cost by 38%, compared to the HVAC system without MicroCSP with an MPC controller. Monte-Carlo simulation results show that the energy cost saving varies from 37% to 42% and from 12% to 47% by considering prediction uncertainties and seasonal variations of the solar irradiation, outdoor temperature, and LMP.
- The optimal control results show the importance of properly sizing TES and sizing MicroCSP for a certain number of thermal zones. Without using TES, both energy saving and cost saving dropped by 16%.

VII. FUTURE WORK

Future work will compare the MPC results from this work with those by using PV panels in terms of energy and energy cost savings. In addition, future work will include experimental implementation of the designed MPC and evaluate the energy cost saving potential for yearly operation of the HVAC system with varying weather conditions.

ACKNOWLEDGMENTS

This work is supported in part by the US National Science Foundation (Grant #1541148), the Richard and Elizabeth Henes Professorship of Mechanical Engineering at Michigan Technological University, and the Institute for Research on Solar and New Energies (IRESEN) in Morocco (reference: InnoTherm-13-MicroCSP).

REFERENCES

[1] EPA. Inventory of U.S. Greenhouse Gas Emissions and Sinks: 1990-2015. (Accessed on 28 January 2018). [Online]. Available: https://www.epa.gov/ghgemissions/inventory-us-greenhouse-gas-emissions-and-sinks-1990-2015.

[2] EIA, 2018. "Electric power monthly with data for november 2017". (Accessed on 18 January 2018). [Online]. Available: https://www.eia.gov/electricity/monthly/current-month/epm.pdf.

[3] EIA. International energy outlook 2017. (Accessed on 18 January 2018). [Online]. Available: https://www.eia.gov/outlooks/aeo/pdf/0383(2017).pdf.

[4] Steinfeld, A., and Palumbo, R., 2001. "Solar thermochemical process technology". *Encyclopedia of physical science and technology,* ***15***(1), pp. 237–56.

[5] Mueller, A., Orosz, M., Narasimhan, A. K., Kamal, R., Hemond, H. F., and Goswami, Y., 2016. "Evolution and feasibility of decentralized concentrating solar thermal power systems for modern energy access in rural areas". *MRS Energy & Sustainability-A Review Journal,* ***3***, p. E4.

[6] Giovannelli, A., 2015. "State of the art on small-scale concentrated solar power plants". *Energy Procedia,* ***82***, pp. 607–614.

[7] Shahidehpour, M., Yamin, H., and Li, Z., 2002. *Market Operations in Electric Power Systems: Forecasting, Scheduling and Risk Management*. Wiley Online Library.

[8] Chandan, V., and Alleyne, A. G., 2014. "Decentralized predictive thermal control for buildings". *Journal of Process Control,* ***24***(6), pp. 820–835.

[9] Maasoumy, M., and Sangiovanni-Vincentelli, A., 2012. "Total and peak energy consumption minimization of building HVAC systems using model predictive control". *IEEE Design Test of Computers,* ***29***(4), pp. 26–35.

[10] Elliott, M. S., and Rasmussen, B. P., 2008. "Model-based predictive control of a multi-evaporator vapor compression cooling cycle". In 2008 American Control Conference (ACC), pp. 1463–1468.

[11] Mu, B., Li, Y., Salsbury, T. I., and House, J. M., 2015. "Extremum seeking based control strategy for a chilled-water plant with parallel chillers". In ASME 2015 Dynamic Systems and Control Conference.

[12] Razmara, M., Bharati, G. R., Hanover, D., Shahbakhti, M., Paudyal, S., and Robinett, R. D., 2017. "Enabling demand response programs via predictive control of building-to-grid systems integrated with PV panels and energy storage systems". In 2017 American Control Conference (ACC), pp. 56–61.

[13] Sun, C., Sun, F., and Moura, S. J., 2015. "Data enabled predictive energy management of a PV-battery smart home nanogrid". In 2015 American Control Conference (ACC), pp. 1023–1028.

[14] ENOGIA SAS, 2017. DATASHEET: ENOGIA'S ENO-10LT ORC System Fact Sheet. (Accessed on 20 June 2017). [Online]. Available: http://www.enogia.com/images/offer/datasheet-ENO10LT.pdf.

[15] Soltigua - Parabolic Troughs PTMx. (Accessed on 27 August 2017).

[16] Duffie, J. A., and Beckman, W. A., 2013. *Solar engineering of thermal processes*. John Wiley & Sons.

[17] Cooper, P., 1969. "The absorption of radiation in solar stills". *Solar energy,* ***12***(3), pp. 333–346.

[18] Spencer, J., 1971. "Fourier series representation of the position of the sun". *Search,* ***2***(5), pp. 172–172.

[19] Forristall, R., 2003. Heat transfer analysis and modeling of a parabolic trough solar receiver implemented in engineering equation solver. Technical Report, The US National Renewable Energy Laboratory (NREL).

[20] Agenzia Nazionale per le Nuove tecnologie, l'Energia e lo Sviluppo economico sostenibile (ENEA), 2017. Performance test report summary according to EN 12975-2:2006. Technical communication with SOLTIGUA. (Accessed on 22 March 2017).

[21] Drouineau, J., 2017. Technical communication with ENOGIA. (Accessed on 28 August 2017).

[22] Maasoumy, M., Razmara, M., Shahbakhti, M., and Sangiovanni-Vincentelli, A., 2014. "Selecting Building Predictive Control Based on Model Uncertainty". In 2014 American Control Conference (ACC).

[23] Razmara, M., Maasoumy, M., Shahbakhti, M., and Robinett III, R. D., 2015. "Optimal exergy control of building HVAC system". *J. Applied Energy,* ***156***, pp. 555–565.

[24] Razmara, M., Bharati, G., Shahbakhti, M., Paudyal, S., and III, R. D. R., 2016. "Bilevel Optimization Framework for Smart Building-to-Grid Systems". *IEEE Transactions on Smart Grid* (99).

[25] MISO. Midcontinent Independent System Operator. (Accessed on 3 September 2014).

[26] Lofberg, J., 2004. "YALMIP: A toolbox for modeling and optimization in MATLAB". In 2004 IEEE International Symposium on Computer Aided Control Systems Design, pp. 284–289.

[27] Razmara, M., Bharati, G., Hanover, D., Shahbakhti, M., Paudyal, S., and Robinett III, R., 2017. "Building-to-grid predictive power flow control for demand response and demand flexibility programs". *Applied Energy,* ***203***, pp. 128–141.

[28] NREL. NSRDB Data Viewer. (Accessed on 19 Apr. 2017). [Online]. Available: https://maps.nrel.gov/nsrdb-viewer/.